JCB Journal of Cell Biology

ARTICLE

The AAA+ ATPase/ubiquitin ligase mysterin stabilizes cytoplasmic lipid droplets

Munechika Sugihara[1], Daisuke Morito[2,3], Shiori Ainuki[1], Yoshinobu Hirano[4], Kazutoyo Ogino[4], Akira Kitamura[5], Hiromi Hirata[4], and Kazuhiro Nagata[1,2,3]

Mysterin, also known as RNF213, is an intracellular protein that forms large toroidal oligomers. Mysterin was originally identified in genetic studies of moyamoya disease (MMD), a rare cerebrovascular disorder of unknown etiology. While mysterin is known to exert ubiquitin ligase and putative mechanical ATPase activities with a RING finger domain and two adjacent AAA+ modules, its biological role is poorly understood. Here, we report that mysterin is targeted to lipid droplets (LDs), ubiquitous organelles specialized for neutral lipid storage, and markedly increases their abundance in cells. This effect was exerted primarily through specific elimination of adipose triglyceride lipase (ATGL) from LDs. The ubiquitin ligase and ATPase activities of mysterin were both important for its proper LD targeting. Notably, MMD-related mutations in the ubiquitin ligase domain of mysterin significantly impaired its fat-stabilizing activity. Our findings identify a unique new regulator of cytoplasmic LDs and suggest a potential link between the pathogenesis of MMD and fat metabolism.

Introduction

Moyamoya disease (MMD) is a rare cerebrovascular disorder that occurs in all races but mostly in East Asians (Scott and Smith, 2009). It is characterized by bilateral stenosis/occlusion of the intracranial internal carotid arteries, which often results in cerebral infarction and life-threatening hemorrhage from the collateral vessels. To date, the etiology and the pathological mechanism of MMD remain largely unknown, and radical treatment is not established. Genetic studies revealed that a small percentage (0.5–2%) of East Asians carries a missense mutation (R4810K) in the *mysterin* gene (moyamoya stenoocclusive disease–associated AAA+ and RING (really interesting new gene) finger protein, also known as *RNF213*; Kamada et al., 2011; Liu et al., 2011; Morito et al., 2014; Koizumi et al., 2016). This mutation is considered to be responsible for the susceptibility of East Asians to MMD (10-fold higher than that of Caucasians); however, the physiological and pathological roles of the *mysterin* gene and its mutations, including the ones recently identified within Caucasian MMD patients, remain elusive (Cecchi et al., 2014; Koizumi et al., 2016; Raso et al., 2016; Guey et al., 2017).

The *mysterin* gene is conserved in protochordates and vertebrates and is ubiquitously expressed throughout the body in humans and mice (Kamada et al., 2011; Liu et al., 2011). Despite its extraordinarily large molecular size (591 kD), only a few domain structures have been determined in the mysterin protein, namely, two AAA+ (ATPases associated with diverse cellular activities) modules and a single RING finger ubiquitin ligase domain (Fig. 1 A; Liu et al., 2011; Morito et al., 2014). AAA+ proteins commonly form hexameric toroidal complexes and generate mechanical force through structural conversion with ATP binding/hydrolysis cycles to mediate various biophysical processes (e.g., dynein exerts a motor activity; Ogura and Wilkinson, 2001). Mysterin has the ability to form toroidal oligomers and hydrolyze ATP (Liu et al., 2011; Morito et al., 2014), whereas the mechanical process it mediates in cells remains elusive. Ubiquitin ligases covalently modify substrate proteins with the small protein ubiquitin, resulting in their proteolysis or functional regulation (Metzger et al., 2014). Previous studies proposed that mysterin exerts ubiquitylation activity toward a variety of substrate proteins, including itself (autoubiquitylation; Liu et al., 2011; Banh et al., 2016; Scholz et al., 2016; Kotani et al., 2017). To our knowledge, mysterin is the only known protein that exerts both AAA+ ATPase and ubiquitin ligase activities, while how it coordinates the unique combination of enzymatic activities and what role it plays in cells remain elusive.

Mysterin protein shows a diffuse distribution in the cytosol and is partly associated with undetermined intracellular

[1]Faculty of Life Sciences, Kyoto Sangyo University, Kyoto, Japan; [2]Institute for Protein Dynamics, Kyoto Sangyo University, Kyoto, Japan; [3]Core Research for Evolutional Science and Technology, Japan Science and Technology Agency, Kawaguchi, Japan; [4]Department of Chemistry and Biological Science, College of Science and Engineering, Aoyama Gakuin University, Sagamihara, Japan; [5]Laboratory of Molecular Cell Dynamics, Faculty of Advanced Life Science, Hokkaido University, Sapporo, Japan.

Correspondence to Daisuke Morito: morito@med.showa-u.ac.jp; D. Morito's present address is Department of Biochemistry, Showa University School of Medicine, Tokyo, Japan.

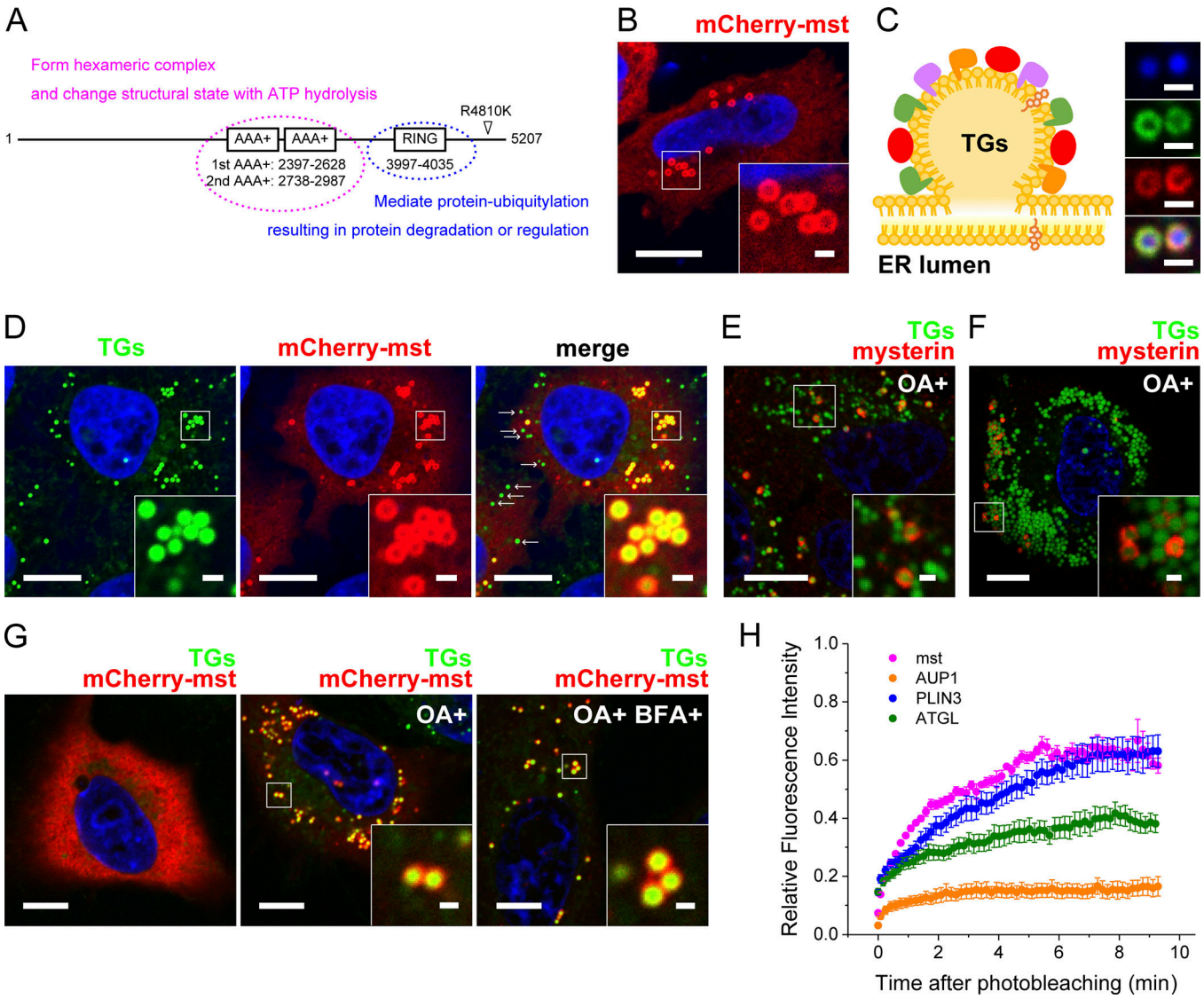

Figure 1. **Mysterin is targeted to LDs. (A)** The major isoform of human mysterin consists of 5,207 amino acids. Mysterin harbors two adjacent AAA+ modules and a single RING finger ubiquitin ligase domain. R4810K is the representative mutation associated with MMD in East Asians. **(B)** Transiently expressed mysterin harboring mCherry at its N terminus (mCherry-mst) partly surrounded putative spherical structures with a diameter of 1 µm in HeLa cells, while the remainder showed a diffuse cytosolic distribution (red). The nuclear chromosome was stained with Hoechst 33342 (blue). The inset shows a magnified image. The scale bars in the original and magnified images indicate 10 and 1 µm, respectively. **(C)** Nascent TGs are stored between the bilayer leaflets of the ER membrane and form spherical LDs on the cytoplasmic side with an encapsulating monolayer membrane and various surface proteins (schematic diagram). The right panels show neutral lipid (blue), endogenous PLIN3 (green), and endogenous ATGL (red) in HeLa cells supplemented with OA. The scale bars indicate 1 µm. **(D)** mCherry-mst surrounded LDs stained with BODIPY 493/503 in HeLa cells (red: mCherry; green: neutral lipid; blue: chromatin). Some LDs were not encircled by mysterin (white arrows). mCherry-mst was associated transiently with LDs or may favor a particular subset of LDs. The insets show magnified images. The scale bars in the original and magnified images indicate 10 and 1 µm, respectively. **(E)** Endogenous mysterin stained with anti-human mysterin antibody (1C9) showed LD targeting (red, mysterin; green, neutral lipid; and blue, chromatin). HeLa cells were treated with OA to enhance LD formation and with interferon-γ to enhance the expression of endogenous mysterin. The inset shows a magnified image. The scale bars in the original and magnified images indicate 10 and 1 µm, respectively. **(F)** Endogenous mysterin in HepG2 cells was stained as described in E (red, mysterin; green, neutral lipid; and blue, chromatin). The inset shows a magnified image. The scale bars in the original and magnified images indicate 10 and 1 µm, respectively. **(G)** mCherry-mst showed only diffuse distribution in HeLa cells in which LDs were disrupted by supplementation with a lipogenesis inhibitor triacsin C for 6 h (left panel; red, mCherry; green, neutral lipid; and blue, chromatin). The removal of triacsin C and supplementation with OA recovered both LDs and the LD distribution of mysterin (middle panel). The recovered LD targeting of mysterin was not affected by supplementation with BFA. The insets show magnified images. The scale bars in original and magnified images indicate 10 and 1 µm, respectively. **(H)** mCherry-mst (cell number = 5), mCherry-AUP1 (n = 5), PLIN3-GFP (n = 7), and GFP-ATGL (n = 8) were overexpressed in HeLa cells supplemented with OA. The fluorescence signals showing toroidal patterns were bleached with intense laser irradiation, and the fluorescence recovery (FRAP) was measured. The data are represented as the means ± SD.

structures (Liu et al., 2011; Morito et al., 2014). Closer microscopic reevaluation in this study revealed that a portion of mysterin specifically encapsulates lipid droplets (LDs), ubiquitous organelles specialized for neutral lipid storage, and stabilizes them through the elimination of an influential lipase, adipose triglyceride lipase (ATGL), from their surfaces. Proper LD targeting of mysterin needs its intrinsic ATPase and ubiquitin ligase activities and is markedly impaired by rare Caucasian MMD mutations in the ubiquitin ligase domain. Our findings identify a unique new component of the cellular fat storage machinery and may suggest a link between the pathogenesis of MMD and fat metabolism.

Results

Mysterin is targeted to LDs

To dissect the subcellular distribution of mysterin, we performed high-resolution fluorescence microscopy with mysterin harboring mCherry at its N terminus (mCherry-mst). Transiently expressed mCherry-mst showed a diffuse distribution throughout the cytosol and partly exhibited toroidal patterns with a diameter of ∼1 µm in HeLa cells (Fig. 1 B). This appearance was reminiscent of medium-sized intracellular vesicles such as lysosomes, endosomes, and LDs. Among them, LDs are the major fat storage sites present in most tissues and provide sources of metabolic energy and fat substances (Walther and Farese, 2012). This small droplet organelle is composed of water-insoluble cores consisting mainly of neutral lipid triglycerides (TGs), an encapsulating phospholipid monolayer membrane that often retains a connection to the ER, and a set of surface proteins with lipogenic, lipolytic, or regulatory functions (Fig. 1 C). The fluorescent staining of neutral lipids with BODIPY 493/503 revealed that mCherry-mst decorated the LD surfaces in HeLa cells (Fig. 1 D) and was more stably detectable when oleic acid (OA; a major fatty acid in vivo) was supplemented with HeLa cells, human embryonic kidney 293T (HEK293T) cells, and human hepatoma HepG2 cells (lipogenesis-dominated condition; Fig. S1, A–C). In addition, these cell lines and human adipocytes endogenously express mysterin (Fig. S1 D), and its targeting to LDs was also detectable (Fig. 1, E and F; note that better visualization of endogenous mysterin requires its up-regulation by interferon stimulation, which was previously reported and reproduced as shown in Fig. S1, E and F; Kobayashi et al., 2015; Ohkubo et al., 2015). Subcellular fractionation supported the distribution of overexpressed and endogenous mysterin in the cytosol and at LDs in HEK293T and HepG2 cells (Fig. S1, G–J). Thus, mysterin is a protein that is targeted to LDs.

Roughly two paths are proposed for protein targeting to LDs: through the ER-LD connection sites (class I) and directly from the cytosol (class II and others; Kory et al., 2016). In the former pathway, some of proteins are first embedded in the ER membrane by their hydrophobic hairpin motif and are then transferred to LDs in a manner that depends on an alternative action of the COPI machinery (Soni et al., 2009; Wilfling et al., 2014). The LD distribution of mCherry-mst was, however, not sensitive to brefeldin A (BFA), an inhibitor of the COPI machinery (Fig. 1 G), in contrast to BFA-sensitive LD distribution of ATGL (previously reported and reproduced in Fig. S1 K). These results suggest that mysterin is not a class I LD protein harboring the hairpin motif. Rather, the considerable distribution of mysterin in the cytosol (e.g., Figs. 1 B and S1 H) and its complete absence in the membrane fraction (Fig. S1, H–J) suggest that mysterin is directly targeted from the cytosol to LDs. Furthermore, mCherry-mst showed substantial FRAP at LDs (Fig. 1 H), suggesting that molecular exchange occurred between LD-targeted (photobleached) and cytosolic (photoactive) species of mCherry-mst. The relatively large maximum recovery proportion and short half-recovery time of mCherry-mst at LDs compared with those of other LD proteins (i.e., ATGL, PLIN3/TIP-47, and AUP1) suggest that the targeting of mysterin to LDs is reversible and fast (Fig. S1, L and M). Overall, mysterin most likely shuttles directly and rapidly between the cytosol and LDs.

Mysterin increases LDs by modulating the lipolytic process

We found that cells transiently overexpressing mCherry-mst formed LDs more extensively than intact (nontransfected) cells (Fig. 2 A). Quantitative analysis of those LDs revealed that the number of LDs and the area occupied by LDs are markedly increased in mysterin-overexpressing cells (Fig. 2 B). Conversely, the depletion of mysterin protein by CRISPR/Cas9-mediated knockout (KO) or siRNA-mediated knockdown resulted in a significantly reduced abundance of LDs despite supplementation with OA (Fig. 2, C and D; and Fig. S2 C; validation of KO/knockdown is shown in Fig. S2, A and B). Reduced TG content in the KO cell lines was also confirmed with the colorimetric TG quantification (Fig. S2 D). These observations suggest that mysterin participates in the maintenance of cellular fat storage.

The abundance of cellular neutral lipids is primarily determined by the balance between lipogenesis and lipolysis in cells, either or both of which might be modulated by mysterin. In other words, mysterin could promote lipogenesis and/or prevent lipolysis to increase fat storage. We reevaluated the positive effect of mysterin on LD abundance in the presence of a lipogenesis inhibitor (triacsin C, an inhibitor of fatty acyl-CoA synthetase) or a lipolysis inhibitor (orlistat, a general lipase inhibitor) to determine which process is affected by mysterin. Overexpression of mCherry-mst retained its effect on LD abundance even when the rate-limiting step of TG synthesis was shut off by the supplementation with triacsin C (Fig. 2, E and F), suggesting that the positive effect of mysterin on LDs does not primarily depend on lipogenesis. By contrast, the inhibition of TG mobilization by orlistat largely negated the negative impact of mysterin KO on LDs (Fig. 2, G and H), suggesting that mysterin increases LDs primarily by interfering with the lipolytic process.

A similar result was obtained in vivo. We previously identified two *mysterin* homologues in zebrafish (*α* and *β*) and demonstrated that the major isoform (*α*) was important for the embryonic development of multiple tissues (Liu et al., 2011; Kotani et al., 2015). Zebrafish larvae form LDs in the head region (Bhandari et al., 2016; reproduced in Fig. S2 E, top panels), and the knockdown of *mysterin-α* by the injection of antisense morpholino oligonucleotide decreased these LDs (Fig. S2 E, second panels). The negative impact of *mysterin-α* knockdown

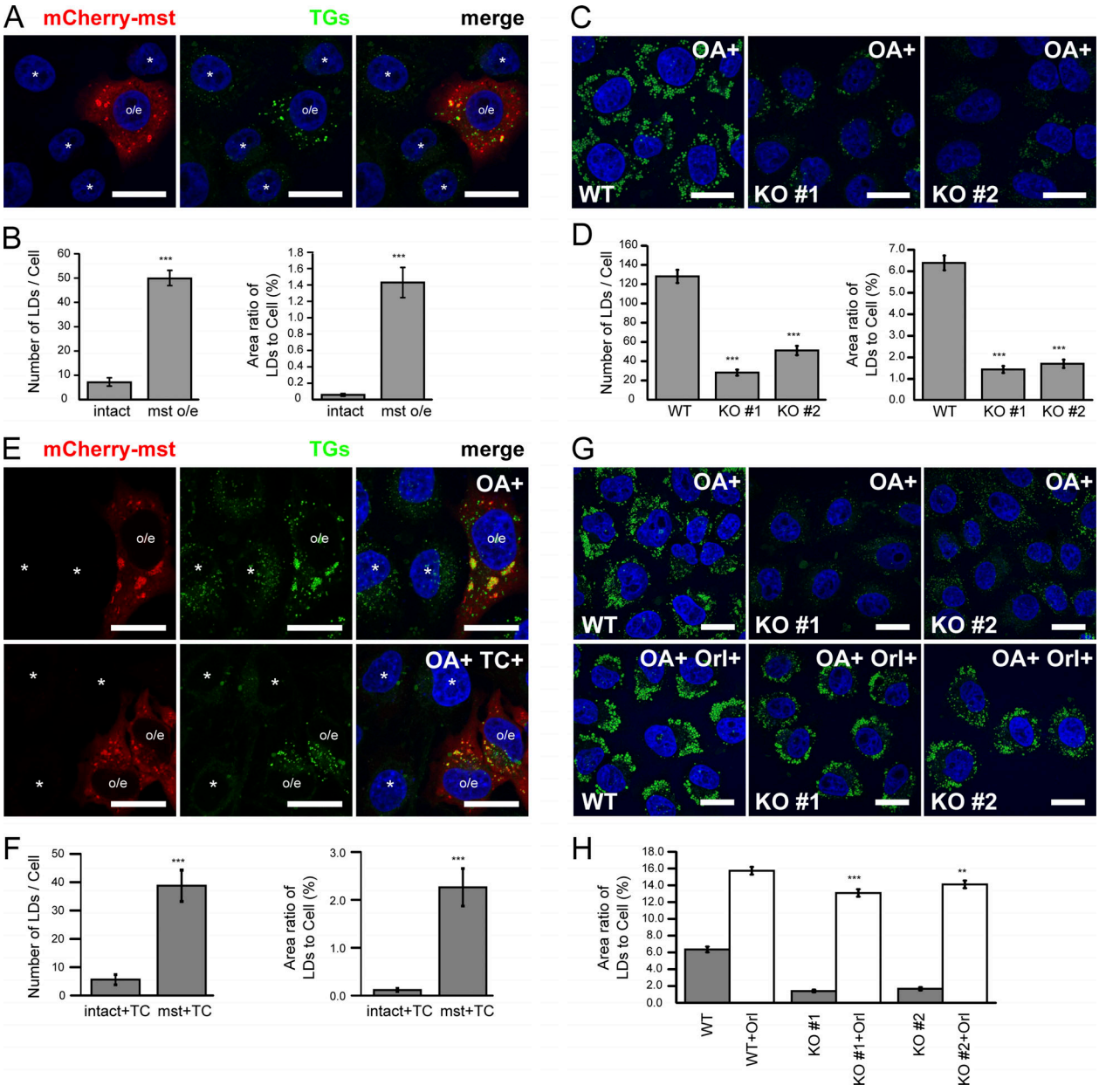

Figure 2. **Mysterin increases LDs by modulating lipolysis. (A)** Although HeLa cells form a small number of LDs at 48 h after medium replacement, the overexpression of mCherry-mst resulted in the enhanced formation of LDs (red, mCherry; green, neutral lipid; blue, chromatin; asterisks, intact cells; and o/e, overexpressing cells). The scale bars indicate 10 µm. **(B)** Quantification of the LD abundance, of which a representative image is shown in A. The number of LDs and the area occupied by LDs were larger in mCherry-mst–overexpressing cells (mst: cell number = 32) than in control cells (intact: *n* = 37). The data are represented as the means ± SEM. ***, P < 0.001 (compared with intact), as analyzed using a Student's two-tailed *t* test. **(C)** Mysterin KO using the CRISPR-Cas9 system in HeLa cells resulted in less LD formation (KO lines #1 and #2) than that in control cells (WT; green, neutral lipid; and blue, chromatin). Basal LD formation was enhanced by OA supplementation. The scale bars indicate 20 µm. **(D)** Quantification of LD abundance in the KO cells for which representative images are shown in C. The number of LDs and area occupied by LDs were dramatically decreased in mysterin KO cells (#1 and #2: cell numbers = 41 and 35, respectively) compared with those in control cells (WT: *n* = 39). The data are represented as the means ± SEM. ***, P < 0.001 (compared with WT), as analyzed using a Student's two-tailed *t* test. **(E)** Triacsin C (TC) treatment for 6 h depleted LDs from HeLa cells even with supplementation with OA (lower panels, cells labeled with asterisks), whereas the overexpression of mCherry-mst retained LDs under the same conditions (lower panels, cells labeled as o/e; green, neutral lipid; and blue, chromatin). The upper panels show cells without triacsin C treatment. The scale bars indicate 20 µm. **(F)** Quantification of the LD abundance, of which representative images are shown in E. The number of LDs and the area occupied by LDs were larger in mCherry-mst–overexpressing cells (mst: cell number = 20) than in control cells (intact: *n* = 17). The data are represented as the means ± SEM. ***, P < 0.001 (compared with intact), as analyzed using a Student's two-tailed *t* test. **(G)** As shown in C, mysterin KO decreased LDs in cells even in the presence of OA (upper panels; green, neutral lipid; and blue, nuclear chromatin), whereas cosupplementation with the general lipase inhibitor orlistat negated the effect of mysterin KO (lower panels). The scale bars indicate 20 µm. **(H)** Quantification of the results for which representative images are shown in G. The data obtained from cells not treated with orlistat (Orl; columns 1, 3, and 5) are the same as those shown in D. The numbers of the analyzed orlistat-treated cells are 45 (WT), 44 (#1), and 40 (#2). The data are represented as the means ± SEM. **, P < 0.01; and ***, P < 0.001 (compared with WT+Orl), as analyzed using a Student's two-tailed *t* test.

on LDs was negated by orlistat, as was the case in HeLa cells (Figs. S2 E, third and fourth panels). Thus, the attenuation of lipolysis by mysterin was reproduced in vivo and is likely conserved across species.

Mysterin eliminates the rate-limiting lipase from LDs

The lipolysis of TGs is mediated in a stepwise fashion by three LD surface lipases: ATGL, hormone-sensitive lipase, and monoacylglycerol lipase (Walther and Farese, 2012). Among them, ATGL is the rate-limiting and most influential lipase (Zimmermann et al., 2004; Zechner et al., 2017). Cells overexpressing mCherry-mst showed markedly decreased ATGL associated with LDs (Fig. 3 A, cells labeled as o/e), while most intact cells showed LDs highly decorated with ATGL (Fig. 3 A, cells labeled with an asterisk). Consistently, mysterin KO cells showed markedly increased ATGL attached to LDs (Fig. 3, B and C), while the protein level of ATGL per se was not changed in the KO cells (Fig. S3 A). Thus, mysterin interfered with the distribution, but not abundance, of ATGL in cells. Other LD proteins such as PLIN3 and AUP1 showed partial colocalization with mCherry-mst (Fig. 3 D and Fig. S3, B–D), while ATGL never demonstrated such a colocalization with mysterin (Fig. 3 E). A sharper contrast was observed under overexpression conditions. Mysterin was always (100%) colocalized with overexpressed PLIN3 and AUP1 (Fig. S3, E and F), while it never (0%) demonstrated colocalization with overexpressed ATGL (as shown in Fig. S5 A). Thus, the eliminative effect of mysterin on the LD surface protein was not indiscriminate. The LD distribution of ATGL should be primarily determined by its influx and efflux from LDs. We monitored the disappearance (efflux) of ATGL at LDs by selectively inhibiting its influx to LDs with BFA supplementation. We found no considerable delay in the ATGL efflux in mysterin KO cells (Fig. S4 A), suggesting that the ATGL elimination by mysterin was not attributed to the acceleration of its efflux from LDs. We also examined the recovery (influx) of ATGL after removal of BFA. HeLa cells were pretreated with BFA for 12 h to completely eliminate ATGL from LDs. The recovery of ATGL after the removal of BFA was more prominent in mysterin KO cells (Fig. S4 B), suggesting that mysterin eliminated ATGL by preventing its influx to LDs. This point was evaluated more precisely by FRAP measurement. The FRAP of GFP-ATGL was significantly larger in mysterin KO cells, indicating that molecular exchange of ATGL at LDs was faster in mysterin KO cells (Fig. S4, C and D). This means that influx, efflux, or both influx and efflux of ATGL at LDs are faster in the KO cells. Along with the findings that the ablation of mysterin positively affected the accumulation of ATGL at LDs (Figs. 3 B), the influx but not efflux of ATGL should primarily be accelerated in the KO cells (i.e., endogenous mysterin presumably reduces ATGL at LDs by preventing its influx to LDs). By contrast, PLIN3-GFP showed just similar fluorescence recovery curves in the WT and mysterin KO HeLa cells, again suggesting that the eliminative effect of mysterin is not indiscriminate (Fig. S4, E and F). To our surprise, the specific exclusive event occurred between mysterin and ATGL was not unidirectional. Overexpression of ATGL conversely eliminated mysterin from LDs (Fig. S5 A), while such an effect was not observed with overexpressed PLIN3 or AUP1 (as shown in Fig. S3, E and F). Thus, it is most likely that mysterin and ATGL specifically compete with each other for LD targeting (Fig. S5 B). However, we did not find a physical interaction between mysterin and ATGL (Fig. S5 C), suggesting that they might interfere with each other through a third factor (e.g., competition for a common anchoring protein that facilitates LD localization of both proteins). The KO of mysterin significantly destabilized LDs, as shown in Fig. 2; however, this effect was negated by the additional knockdown of ATGL by siRNA (Fig. 3 F; the knockdown efficiency is shown in Fig. S5 D). These results suggest that the LD stabilization effect of mysterin is attributed to the specific elimination of the rate-limiting lipase ATGL from LDs.

Role of the enzymatic activity of mysterin and its impairment by MMD mutations

Mysterin exerts ATPase and ubiquitin ligase activities with two AAA+ domains and a RING finger domain, respectively (Liu et al., 2011; Morito et al., 2014). We tested the involvement of these activities in LD formation. Fig. 4 A shows a schematic representation of the enzymatic mutants examined in this study. A1A2 and B1B2 each carry two essential mutations in the ATP binding motifs (A motifs) and Mg binding motifs (B motifs) essential for ATP hydrolysis, respectively. Thus, these mutants lost the ATP binding activities (A1A2) and ATP hydrolysis activities (B1B2; Morito et al., 2014). We found that both mutants harboring mCherry at their N termini were no longer targeted to LDs and diffused throughout the cytosol (Fig. 4 B), indicating an essential involvement of the ATP binding and hydrolysis activities in the LD targeting of mysterin. Given the analogy with a certain type of AAA+ protein, the LD association and dissociation of mysterin are presumably synchronized to its ATP binding and hydrolysis cycles (see Discussion section).

The mutant lacking the RING finger ubiquitin ligase domain (ΔRING) also showed an altered distribution; however, its modality was different from that observed with the ATPase mutants. The ΔRING mutant harboring mCherry at its N terminus (mCherry-ΔRING) showed amorphous aggregate-like patterns and lost the LD distribution in most cells (~80%; Fig. 4 C, left panel), although a degree of the LD distribution was detectable in a small proportion of cells (~20%; Fig. 4 C, right panel). The ΔRING mutant that was successfully targeted to LDs retained the exclusive effect against ATGL (Fig. S6 A), suggesting that the elimination of ATGL did not occur through ubiquitylation of ATGL by mysterin. Rather, the ubiquitin ligase activity of mysterin appeared to be involved in its self-maintenance or self-regulation for the proper LD distribution. Our previous finding that the ubiquitin ligase activity of mysterin was exerted toward itself (autoubiquitylation), which was lost in the ΔRING mutant (Liu et al., 2011), may support the self-maintenance/self-regulation model.

As expected, the LD distribution of mysterin and its fat stabilization effect were correlated with each other. The A1A2 and B1B2 mutants did not show any positive effect on LD abundance (Fig. 4 D). The ΔRING mutant, which showed amorphous aggregate-like patterns (agg), also lost the positive effect on LDs, while the small proportion of the mutant that retained the LD

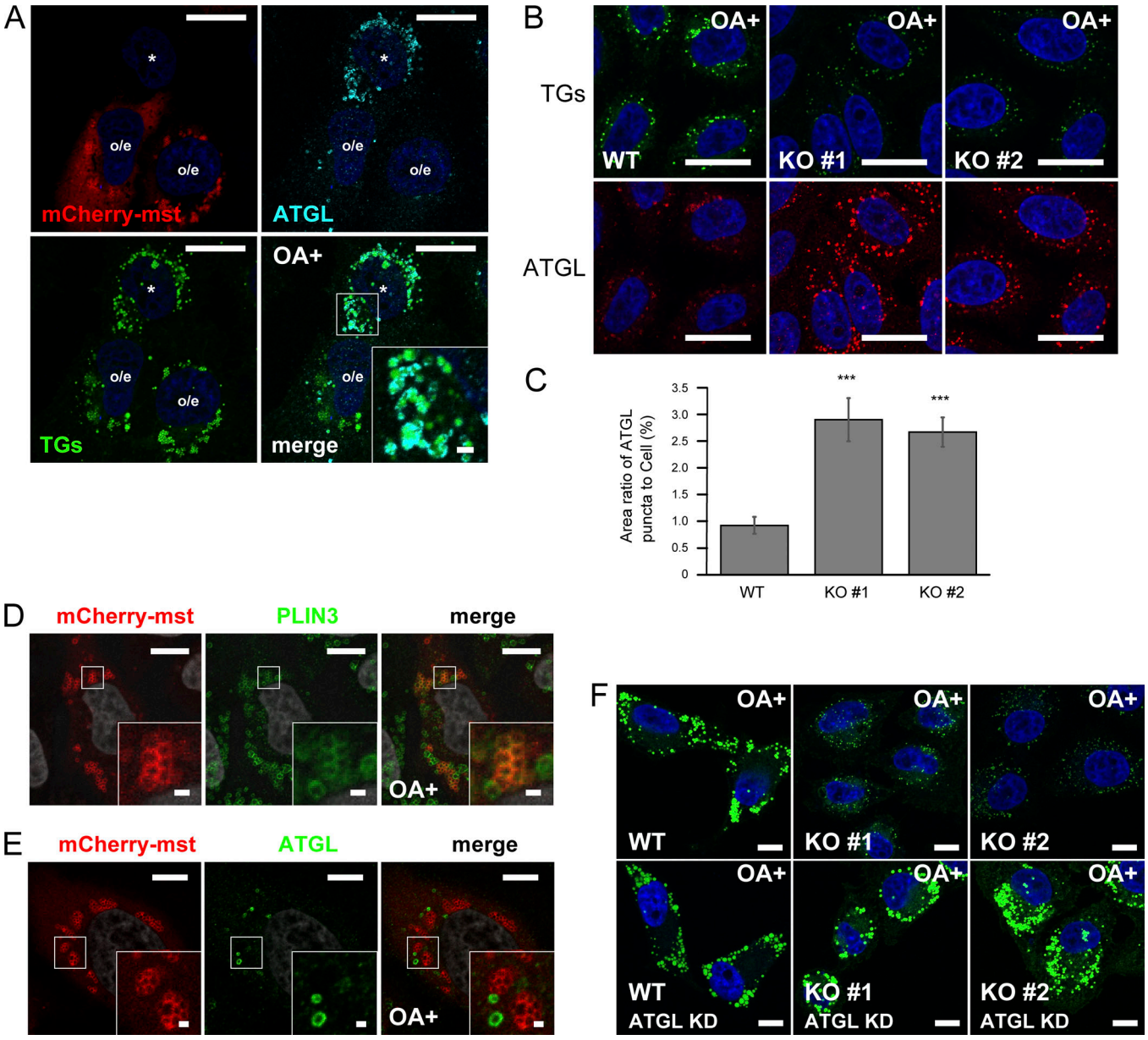

Figure 3. **Mysterin specifically eliminates ATGL from LDs. (A)** LD formation in HeLa cells was saturated by supplementation with OA (red, mCherry; green, neutral lipid; blue, chromatin; and cyan, endogenous ATGL). The overexpression of mCherry-mst (labeled as o/e) resulted in markedly less decoration of LDs with ATGL in comparison to those in the intact cells (labeled with an asterisk). The inset shows magnified image. The scale bars in the original and magnified images indicate 10 and 1 µm, respectively. **(B)** Mysterin KO decreased LDs in HeLa cells (upper panels), whereas the decorative distribution of endogenous ATGL at LDs was conversely increased in the KO cells (lower panels; green, neutral lipid; blue, chromatin; and red, endogenous ATGL). The basal LD formation was enhanced with OA supplementation. The scale bars indicate 20 µm. **(C)** Quantification of the results for which representative images are shown in B. Area occupied by ATGL puncta was determined, and its ratio to the entire cell is represented as the mean ± SEM. ***, $P < 0.001$ (compared with WT), as analyzed using a Student's two-tailed *t* test. The numbers of analyzed cells are 20 (WT), 20 (KO #1), and 15 (KO #2). **(D and E)** HeLa cells overexpressing mCherry-mst were stained with anti-PLIN3 or anti-ATGL antibody (red, mCherry; green, endogenous PLIN3/ATGL; and gray, chromatin). LD formation was enhanced by the supplementation with OA. The insets show magnified images. The scale bars in the original and magnified images indicate 10 and 1 µm, respectively. **(F)** Mysterin KO decreased LDs in HeLa cells even in the presence of OA (upper panels; green, neutral lipid; and blue, chromatin), whereas the knockdown (KD) of ATGL by siRNA (#1) negated the effect of mysterin KO (lower panels). The scale bars indicate 10 µm.

localization (LD) showed a degree of the LD stabilization effect (Fig. 4 D). Thus, the two enzymatic activities of mysterin are both involved in its fat stabilization function.

Involvement of the RING finger domain in the metabolic function of mysterin could be particularly important, considering the MMD etiology. Four mutations at conserved cysteine/histidine residues in the RING finger domain were recently identified in rare Caucasian MMD cases (C3997Y, H4014N, C4017S, and C4032R; shown in Fig. 4 E; Cecchi et al., 2014; Raso et al., 2016; Guey et al., 2017). We found that all four mutants harboring the 3×FLAG tag at their C termini showed impaired LD targeting and aggregate formation highly similar to those

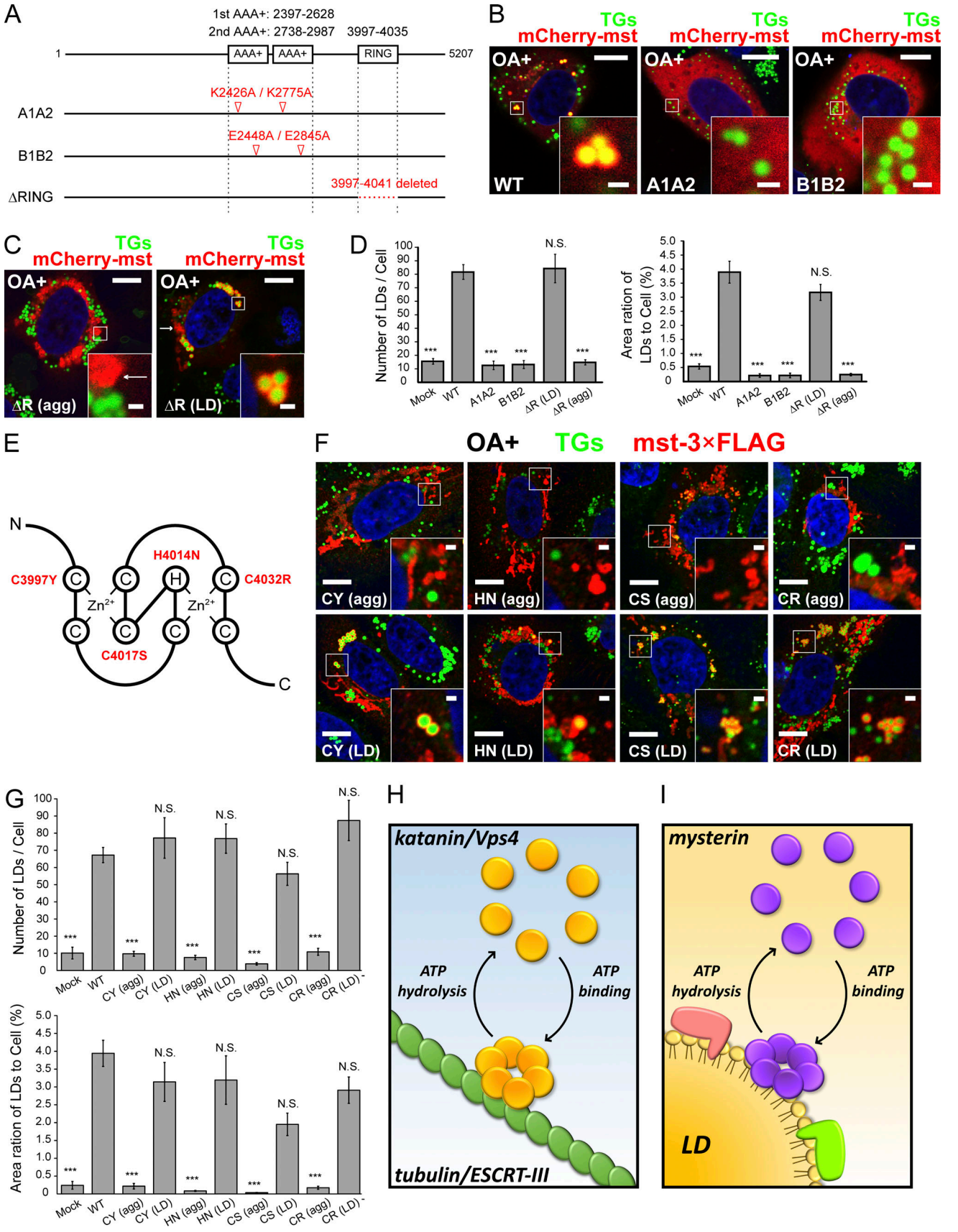

Figure 4. **Evaluation of enzymatic and pathogenic mutants. (A)** Primary structures of the enzymatic mutants tested. Each mutant harbors mCherry at its N terminus (indicated by mCherry-). **(B)** Mutants harboring two mutations in the ATP binding motifs (A1A2), and Mg binding motifs essential for the ATP

observed with the ΔRING mutant (Fig. 4 F). These mutants lost metabolic effects as well (Fig. 4 G), suggesting the pathogenic relevance of the abnormal LD metabolism in Caucasian MMD. By contrast, other MMD mutations, such as East Asian R4810K in the C-terminal region with no predicted functional structure and East Asian/Caucasian D4013N at a nonconserved residue in the RING finger domain (Liu et al., 2011), did not cause any detectable anomalies (Fig. S6, B and C). Such a lack of an effect is most likely attributable to their putative structurally nonessential positions. In addition, the uneven magnitudes of the molecular effects of these mutations could explain their divergent pathogenic effects in MMD (see Discussion section).

Discussion

Through a detailed exploration of the subcellular distribution of mysterin, we ultimately found that this protein is targeted to LDs and serves as a positive regulator of cellular fat storage by selectively eliminating ATGL from LDs. Multistep TG mobilization initiated by ATGL occupies a key position in the cellular/organismal energy metabolism and is regulated by multiple factors/pathways, including those stimulated by catecholamines and insulin (Zechner et al., 2017). Although to which extent and how mysterin contributes to the regulation of cellular/organismal lipid metabolism presently remains elusive, the observation that the knockdown/KO of endogenous mysterin caused significant fat loss in cells suggests an involvement of mysterin in the maintenance of fat storage in vivo.

The LD targeting and fat-stabilizing effect of mysterin required its enzymatic activities. This fact offered some clues to understand the molecular mechanism underlying the metabolic function of mysterin. Unlike most AAA+ proteins that form stable oligomers (mostly hexamers), mysterin dynamically changes its oligomeric (presumably hexameric) state. Mysterin formed an oligomer upon binding with ATP at the first AAA+ module and disassembled upon the hydrolysis of another ATP at the second AAA+ module (Fig. S6 D; Morito et al., 2014). The mysterin A1A2 and B1B2 mutants partially stall in the monomer and oligomer states because of the loss of their ATP binding and hydrolysis activities, respectively (Morito et al., 2014). These mutants commonly showed impaired targeting to LDs (Fig. 4 B), suggesting that the LD targeting of mysterin is not merely determined by its static state (i.e., monomer or oligomer) but is regulated through active cycles of ATP binding/hydrolysis. The cyclic modality of the oligomerization of mysterin resembled that of a few exceptional AAA+ members. The ATP-binding form of katanin and Vps4 assemble on target protein complexes, such as microtubules and the ESCRT-III complex, respectively (Fig. 4 H; Ogura and Wilkinson, 2001). They mediate disassembly of those target complexes upon ATP hydrolysis and return to the diffusive monomer forms (Fig. 4 H). Mysterin could similarly assemble on target LDs (or surface protein) and dissociate being synchronized with the ATP binding/hydrolysis cycles (Fig. 4 I). The vast cytosolic pool of mysterin (e.g., Figs. 1 B and S1 H), its contrasting absence in the membrane fraction (Fig. S1, H–J), and its rapid shuttling between the cytosol and LDs (Fig. 1 H) also support the cyclic model (Fig. 4 I). In the cases of katanin and Vps4, they directly bind to their substrate complexes and mediate their disassembly. However, we found no physical interaction between mysterin and ATGL (Fig. S5 C) and no obvious acceleration of the efflux of preexisting ATGL at LDs (Figs. S4 A). Even if mysterin exerts an activity like that of katanin and Vps4, its direct target should not be ATGL. A plausible scenario is that mysterin and ATGL compete with each other for binding to a common anchoring protein that facilitates the LD localization of both proteins (Fig. S5 B). Mysterin may affect the putative anchoring protein with its AAA+ activity and prevent the ATGL influx to LDs. Conversely, ATGL could occupy the anchoring protein, and it eliminates mysterin from LDs. Further cell biological/biophysical verifications of the present model and dissection of the mechanical process through which mysterin eliminates ATGL are warranted.

hydrolysis (B1B2) showed diffuse distribution despite the obvious LD formation in mysterin KO HeLa cells #1 supplemented with OA (red, mCherry-WT/A1A2/B1B2; green, neutral lipid; and blue, chromatin). The insets show magnified images. The scale bars in original and magnified images indicate 10 and 1 µm, respectively. **(C)** The mutant lacking the RING finger domain (ΔRING) showed amorphous aggregate-like patterns in most (∼80%) cells (left panels) but retained LD targeting to some extent in a minority (∼20%) of cells (right panels; red, mCherry-ΔRING; green, neutral lipid; and blue, chromatin). The cells did not express endogenous mysterin (KO #1 HeLa) and were treated with OA. The insets show magnified images. The scale bars in original and magnified images indicate 10 and 1 µm, respectively. **(D)** Mysterin KO #1 HeLa cells were treated with OA for 16 h to saturate LD formation. OA was then removed, and the cells were treated with triacsin C for 6 h to shut off the lipogenesis. The number and relative area of LDs were quantified. Cells showing the LD targeting of mCherry-ΔRING (ΔR (LD)) retained LDs, whereas those showing aggregate-like patterns (ΔR (agg)) lost their LD-retention activity. The numbers of quantified cells are 30 (mock), 30 (WT), 30 (A1A2), 30 (B1B2), 16 (ΔR (LD)), and 30 (ΔR (agg)). All the quantified data are represented as the means ± SEM. ***, $P < 0.001$ (compared with WT), as analyzed using a Student's two-tailed *t* test. **(E)** Mysterin most likely harbors the HC subtype of the RING finger domain, in which eight conserved cysteine/histidine residues chelate with two zinc ions. Four of these residues were mutated in rare Caucasian MMD cases (C3997Y, H4014N, C4017S, and C4032R). **(F)** The C3997Y (CY), H4014N (HN), C4017S (CS), and C4032R (CR) mutants harboring FLAG tags at their C termini showed aggregate-like patterns in most (∼80%) cells (upper panels) but retained LD targeting to some extent in a minority (∼20%) of cells (lower panels; red, FLAG; green, neutral lipid; and blue, chromatin). The cells did not express endogenous mysterin (KO #1 HeLa) and were treated with OA. The insets show magnified images. The scale bars in original and magnified images indicate 10 and 1 µm, respectively. **(G)** Mysterin KO #1 HeLa cells were treated with OA for 16 h to saturate LD formation. OA was then removed, and the cells were treated with triacsin C for 6 h to shut off the lipogenesis. The number and relative area of LDs were quantified. Cells showing the LD targeting of each mutant (LD) retained LDs, whereas those showing aggregate-like patterns (agg) lost their LD-retention activity. The numbers of quantified cells are 30 (agg) and 10 (LD) for each mutant. All the quantified data are represented as the means ± SEM. ***, $P < 0.001$ (compared with WT), as analyzed using a Student's two-tailed *t* test. **(H)** Katanin and Vps4 assemble on their substrates microtubules and the ESCRT-III complex, respectively, upon ATP binding. They dissociate after disassembling the substrate complexes upon ATP hydrolysis. **(I)** Given the analogy with katanin/Vps4, mysterin could assemble on LDs (or surface proteins) upon ATP binding, mediate a mechanical process upon ATP hydrolysis to eliminate ATGL from LDs, and return to the diffusive monomer forms.

The LD targeting of mysterin was affected by its intrinsic ubiquitin ligase activity. The ΔRING and MMD cysteine/histidine mutants showed substantial detachment from LDs and formation of aggregate-like pattern (Fig. 4, C and F), suggesting a possibility that the ubiquitin ligase activity of mysterin toward itself (autoubiquitylation) exerts a self-maintenance or self-regulatory function such as those found in several ubiquitin ligases (Baldridge and Rapoport, 2016). Elucidation of autoubiquitylation modalities, such as modification site, type of ubiquitin chain, and its effect on molecular behavior of mysterin, is warranted to understand the self-maintenance/regulation of mysterin, which could play significant role in the regulation of cellular/organismal fat metabolism as well as the molecular pathogenesis of MMD.

From the perspective of MMD, the present findings were hardly anticipated in advance. Previous epidemiological studies did not link MMD with any metabolic anomalies such as obesity and dyslipidemia (Scott and Smith, 2009). Histopathological studies showed hyperplasia of vascular smooth muscle cells and luminal thrombosis at the lesion, whereas no atherosclerotic changes were typically found (Scott and Smith, 2009). Thus, MMD has not been considered to be closely related to lipid metabolism. Nevertheless, the current findings that multiple MMD mutations in the RING finger domain impair the metabolic function of mysterin suggest a potential link between MMD and fat anomaly. A range of human disorders, including cardiovascular disorders, is linked to dysfunction and/or dyscontrol of LDs (often caused by mutant LD proteins) in various cells/tissues (Krahmer et al., 2013); however, in MMD, it is not even known which cells/tissues (e.g., vascular endothelial, smooth muscle, endothelial progenitor, or immune cells) form the primary lesion (Scott and Smith, 2009). Further studies in vivo and in vitro are highly warranted to identify the responsible cells/tissues and the contribution of metabolic anomaly in the pathogenesis of MMD. Alternatively, the aggregate-like structure of mislocalized mysterin mutants may exert cytotoxic effects, as was seen in many neurodegenerative disorders (Labbadia and Morimoto, 2015).

Unlike prominent molecular effects of the Caucasian cysteine/histidine mutations in the RING finger domain, the East Asian R4810K mutation and East Asian/Caucasian D4013N mutation in putative nonessential sites did apparently not alter the metabolic function of mysterin. This fact could explain the degrees of genetic penetrance (severities of pathogenicity) of the mutations. The carriers of R4810K and D4013N are susceptible to MMD but did not always develop it (i.e., their genetic penetrance is very low/incomplete), while all known carriers of the cysteine/histidine mutations developed MMD (i.e., their genetic penetrance is presumably very high/complete; Kamada et al., 2011; Liu et al., 2011; Cecchi et al., 2014; Raso et al., 2016; Guey et al., 2017). R4810K and D4013N may exert only a modest or latent effect on the metabolic function of mysterin and require additional environmental and/or genetic factors (e.g., inflammation) to trigger MMD, as was repeatedly discussed in previous epidemiological and genetic studies (Scott and Smith, 2009; Koizumi et al., 2016).

Materials and methods

Cells, transfection, and treatments

HeLa (Kyoto), HEK293T, and HepG2 cells were maintained at 37°C with 7% CO_2 in DMEM (Gibco) supplemented with 10% fetal bovine serum (Sigma) and a penicillin/streptomycin mixture (final 100 U/ml and 100 µg/ml, respectively; Nacalai Tesque). Human visceral preadipocytes (Lonza) were maintained and differentiated into mature adipocytes with the PGM-2 Bullet Kit (Lonza) according to the manufacturer's instructions. Plasmids and siRNAs were transfected into cells using Polyethylenimine MAX (Polysciences) and RNAiMAX (Thermo Fisher Scientific), respectively. OA (Merck) was conjugated to BSA (fatty acid and endotoxin free; Sigma) at a molar ratio of 6:1 in PBS before use. Cells were treated with the OA–BSA complex containing a final concentration of 200–400 µM OA or with a corresponding dose of BSA alone for 16–24 h. Triacsin C (Sigma) and orlistat (AdooQ BioScience) were diluted in DMSO and added to the medium at final concentrations of 5 µM for 6–24 h and of 100 µM for 24–48 h, respectively. Interferon-γ (PBL Assay Science) was added at the concentrations indicated in the figures for 24 h. BFA (Nacalai Tesque) was added at a final concentration of 5 µg/ml for 6–12 h.

Plasmids and siRNAs

WT and mutants of mysterin harboring three tandem FLAG epitopes at its C terminus (mst-3×FLAG) and EGFP at its N terminus (EGFP-mst) were described previously (Liu et al., 2011; Morito et al., 2014). The C3997Y (TGC to TAC), H4014N (CAC to AAC), C4017S (TGC to TCC), and C4032R (TGC to CGC) mutants were created using the PrimeSTAR Mutagenesis Basal Kit (TaKaRa). For comprehensive fluorescence imaging analysis, WT and mutant mst-3×FLAGs were digested at the NheI and NotI sites and subcloned into pIRESpuro4 n-mCherry (kind gift from Shigeo Murata, Graduate School of Pharmaceutical Science, The University of Tokyo, Tokyo, Japan). The multicloning site (MCS) of this plasmid was modified in advance to match the reading frames of the vector-encoded mCherry and subcloned mst-3×FLAGs (sequence of the modified MCS following mCherry: 5′-GAATTCAATCTAGAAAGC TTGGTACCGGGCCCGGATCCAGATCTGATATCCTCGAGCCCTATA GTGAGTCGTATTAGCGGCCGC-3′) and was digested at the XbaI and NotI sites before subcloning. The peGFP-N1-ATGL was a kind gift from Catherine Jackson (Institut Jacques Monod, Université Paris Diderot, Paris, France). The mCherry-AUP1/pcDNA was a kind gift from Hidde Ploegh (Whitehead Institute, Massachusetts Institute of Technology, Cambridge, MA). The TIP-47/PLIN3-GFP was a kind gift from Stefan Höning (Institute of Biochemistry I, University of Cologne, Cologne, Germany). The siRNAs targeting human mysterin were purchased from Ambion (#1: s33568: 5′-CGU AUGAGCUCACAACCGATT-3′ and 5′-UCGGUUGUGAGCUCAUAC GTT-3′; #2: s33658: 5′-CAGCUGCUGUGAAAAACGATT-3′ and 5′-UCGUUUUUCACAGCAGCUGCA-3′). The siRNAs targeting human ATGL were purchased from Invitrogen (#1: PNPLA2HSS125980 [3_RNAI]: 5′-GCGAGAAGACGUGGAACAUCUCGUU-3′ and 5′-AAC GAGAUGUUCCACGUCUUCUCGC-3′; #2: PNPLA2HSS183700 [3_RNAI]: 5′-GAGAAUGUCAUUAUAUCCCACUUCA-3′ and 5′-UGA AGUGGGAUAUAAUGACAUUCUC-3′; #3: PNPLA2HSS183701 [3_RNAI]: 5′-ACCUGCCACUCUAUGAGCUUAAGAA-3′ and 5′-UUC UUAAGCUCAUAGAGUGGCAGGU-3′).

Antibodies

Anti-human mysterin mouse monoclonal antibodies (1D6 and 1C9) were generated as previously described (kindly shared by Seiji Takashima, Graduate School of Medicine, Osaka University, Osaka, Japan; Kotani et al., 2017). Other antibodies were purchased, namely, anti-human PLIN3 mouse monoclonal antibody (sc-390169; Santa Cruz), anti-human ATGL rabbit polyclonal antibodies (for immunostaining, sc-67355; Santa Cruz; for immunoblot, #2138S; Cell Signaling), anti-human AUP1 rabbit polyclonal antibody (HPA007674; Atlas Antibodies), anti-human tubulin rabbit monoclonal antibody (41117; Millipore), anti-rabbit GAPDH mouse monoclonal antibody (5G4; Hy Test), and anti-FLAG M2 mouse monoclonal antibody (F1804; Sigma).

CRISPR-Cas9 system

Short duplex DNAs targeting the coding region of human mysterin (5′-CACCTTGGACGGTCCAGGAGGCTT-3′ and 5′-AAACAAGCCTCCTGGACCGTCCAA-3′), of which the sequences were specified with the CRISPR Search and Design Tool (Thermo Fisher Scientific), were cloned into pSpCas9(BB)-2A-Puro (PX459) V2.0 (kind gift from Feng Zhang, Broad Institute of MIT and Harvard, Cambridge, MA; Addgene plasmid #62988). The vector was transfected into HeLa cells, which were maintained in the presence of 1 µg/ml puromycin for 7 d. The surviving cells were diluted and cultured, and cells forming colonies were isolated and validated (#1 and #2; also see Fig. S3 A).

Cell fractionation

Cell fractionation was performed with the Lipid Droplet Isolation Kit (Cell Biolabs) according to the manufacturer's instructions. 1/200, 1/60, 1/200, and 1/200 (Fig. S1 H); 1/250, 1/30, 1/250, and 1/250 (Fig. S1 I); or 1/200, 1/30, 1/200, and 1/200 (Fig. S1 J) volumes of total, LD, cytosol, and membrane/cytoskeleton fractions, respectively, were subjected to immunoblotting analysis.

Immunoblotting

Samples were prepared as previously described using the cell fractionation procedure or directly from cells lysed with 1% NP-40 containing lysis buffer. The samples were separated by SDS-PAGE using a 5% or ∼3–10% gradient acrylamide gel (ATTO) and transferred to a polyvinylidene difluoride (Merck Millipore) membrane for 1.5 h at 75 V and 4°C. The membrane was blocked using Blocking One (Nacalai Tesque) for 1 h at room temperature and then incubated sequentially with primary (mostly used at 1/200) and secondary antibodies (mostly used at 1/1,000) diluted in Can Get Signal (TOYOBO). Detection was performed via the chemiluminescence method.

Immunostaining and data acquisition

Cells were immobilized with 4% paraformaldehyde (Nacalai Tesque) for 10 min at room temperature, permeabilized with 50 µg/ml digitonin for 5 min, and then washed with PBS. After the incubation with Blocking One for 1 h at room temperature, cells were incubated sequentially with primary and fluorescence-conjugated secondary antibodies (Alexa Fluor 647 goat anti-mouse IgG[H+L]; Alexa Fluor 647 goat anti-rabbit IgG [H+L]; and Alexa Fluor 555 goat anti-mouse IgG[H+L]); each incubation was followed by PBS washing. LDs were stained with BODIPY 493/503 (added simultaneously with secondary antibodies; Thermo Fisher Scientific) and LipiDye (added simultaneously with secondary antibodies or after the cell fractionation; Funakoshi). The nucleus was stained using Hoechst 33342 (Thermo Fisher Scientific). Fluorescence images were obtained at room temperature by confocal microscopy (LSM 700; Carl Zeiss) through a Plan-Apochromat 100×/1.46 oil differential interference contrast (UV) VIS-IR (Carl Zeiss) using ZEN software.

FRAP measurement in live cells

FRAP experiments were performed on an LSM 700 (Carl Zeiss) through a Plan-Apochromat 63×/1.4-NA oil immersion objective (Carl Zeiss) using ZEN software. GFP-ATGL and PLIN3-GFP in HeLa cells were excited at 488 nm and photobleached at 488/555 nm. mCherry-mst and mCherry-AUP1 were excited at 555 nm and photobleached at 488/555 nm. The main beam splitter (MBS405/488/555/639) was used. GFP or mCherry fluorescence was collected using the variable secondary dichroic beam splitter at 493–1,000 or 578–1,000 nm, respectively. The pinhole sizes were set to 69 µm for GFP or 79 µm for mCherry. The X- and Y-scanning sizes were each 512 pixels. The interval time for image acquisition was set to 10.0 s. The photobleaching period was 15 s. The relative fluorescence intensity (RFI) at time t was measured using ZEN software and calculated using Eq. 1.

$$RFI = \frac{I_{BL}(t) - I_{bg}(t)}{I'_{BL} - I'_{bg}}. \quad (1)$$

In Eq. 1, $I_{BL}(t)$ and $I_{bg}(t)$ are the intensities measured at time t in the photobleached region and the background region, respectively. I'_{BL} and I'_{bg} are the intensities measured before photobleaching of the bleached and the background region, respectively. $I_{bg}(t)$ and I'_{bg} were measured in the region without cells.

The recovery curve of RFI was fitted with a one-component exponential recovery model (Eq. 2) using Origin 2017 software (OriginLab Corp.).

$$I(t) = I_0 + A\left(1 - e^{-kt}\right). \quad (2)$$

In Eq. 2, $I(t)$ is the intensity at time t, I_0 is the baseline, A is the coefficient of exponential recovery, k is the recovery rate, and the maximum recovery proportion (I_{max}) is defined as $I_0 + A$. The half-recovery time is calculated as $-(\ln 0.5)/k$. In the analyses of PLIN3 and ATGL (Fig. S4, C–F), the lowest decrease of fluorescence intensity just after the photobleaching (the baseline) was determined using 4% paraformaldehyde–fixed cells expressing PLIN3-GFP. To directly show the mobile proportion, the RFI was normalized using the lowest fluorescence intensity (normalized RFI).

Colorimetric TG quantification

3×10^6 HeLa cells were suspended in 250 µl of PBS containing 1% Triton X-100. The supernatant was subjected to the colorimetric TG quantification assay (Serum Triglyceride Quantification Kit; CELL BIOLABS). The TG density shown in Fig. S2 is that in the supernatant.

Zebrafish and treatments

The zebrafish study was approved by the Animal Ethics Committee of Aoyama Gakuin University and performed according to the guidelines set forth by the same university. The morpholino antisense oligonucleotide was injected at the one- to two-cell stage as previously described (Kotani et al., 2015). Orlistat (AdooQ BioScience) was solved in DMSO at 100 mM and bath-applied to zebrafish larvae at a final concentration of 1 mM in embryo medium E3 containing 5 mM NaCl, 0.17 mM KCl, 0.33 mM $CaCl_2$, and 0.33 mM $MgSO_4$ at the beginning of 1 d postfertilization (dpf). Zebrafish larvae were fixed at 3 dpf in 4% paraformaldehyde/PBS at 4°C for 40 h, each washed twice in PBST (PBS containing 0.1% Tween 20) for 5 min, and stained in 0.3% (wt/vol) oil red O (Wako) in 60% 2-propanol/water for 3 h. The larvae were then rinsed three times in PBST for 5 min, mounted in 75% glycerol, and subjected to image acquisition using Axioplan2 (Carl Zeiss).

Quantification and statistical analysis

The number and relative area of LDs (and its associating proteins) were analyzed with ImageJ (Wayne Rasband and NIH). All data are represented as the mean ± SEM, except for those obtained by FRAP analysis, which are represented as the mean ± SD. The statistical significance was evaluated using Student's two-tailed *t* test. $P < 0.05$ was considered statistically significant. The data distribution was assumed to be normal, but this was not formally tested.

Online supplemental material

Fig. S1 shows the distribution and dynamics of mysterin at LDs (fluorescence imaging, the expression of mysterin in different cell types and upon interferon stimulation, cell fractionation, and FRAP analysis). Fig. S2 shows the fat reduction by KO and knockdown of endogenous mysterin in cells and zebrafish. Figs. S3–S5 show comparative analyses of the effects of mysterin on ATGL, PLIN3, and AUP1 (fluorescence imaging, FRAP analysis, and a model of mutually exclusive effects of mysterin and ATGL). Fig. S6 shows the molecular behaviors of enzymatic and disease susceptibility mutants of mysterin.

Acknowledgments

We thank Kenshiro Sakata, Kanami Moriya, and Masataka Kinjo for their expert help. We thank Shigeo Murata, Shoshiro Hirayama, Seiji Takashima, Osamu Tsukamoto, Hidde Ploegh, Catherine Jackson, and Stefan Höning for sharing valuable reagents. We also thank Akira Miyazaki for kind support.

The study was supported by KAKENHI (grant 15K07062 to D. Morito), CREST, and the Takeda Science Foundation (to K. Nagata).

D. Morito and K. Nagata have a patent pending related to the procedure for mysterin knockdown. The authors declare no further competing financial interests.

Author contributions: D. Morito designed the study and wrote the manuscript with input from the other authors under the supervision of K. Nagata. M. Sugihara, S. Ainuki, and D. Morito performed the cell biological experiments. Y. Hirano, K. Ogino, and H. Hirata performed the zebrafish experiments. A. Kitamura analyzed the FRAP data.

Submitted: 20 December 2017
Revised: 26 June 2018
Accepted: 8 January 2019

References

Baldridge, R.D., and T.A. Rapoport. 2016. Autoubiquitination of the Hrd1 Ligase Triggers Protein Retrotranslocation in ERAD. *Cell.* 166:394–407. https://doi.org/10.1016/j.cell.2016.05.048

Banh, R.S., C. Iorio, R. Marcotte, Y. Xu, D. Cojocari, A.A. Rahman, J. Pawling, W. Zhang, A. Sinha, C.M. Rose, et al. 2016. PTP1B controls non-mitochondrial oxygen consumption by regulating RNF213 to promote tumour survival during hypoxia. *Nat. Cell Biol.* 18:803–813. https://doi.org/10.1038/ncb3376

Bhandari, S., J.N. Lee, Y.-I. Kim, I.-K. Nam, S.-J. Kim, S.-J. Kim, S. Kwak, G.-S. Oh, H.-J. Kim, H.J. Yoo, et al. 2016. The fatty acid chain elongase, Elovl1, is required for kidney and swim bladder development during zebrafish embryogenesis. *Organogenesis.* 12:78–93. https://doi.org/10.1080/15476278.2016.1172164

Cecchi, A.C., D. Guo, Z. Ren, K. Flynn, R.L.P. Santos-Cortez, S.M. Leal, G.T. Wang, E.S. Regalado, G.K. Steinberg, J. Shendure, et al.; University of Washington Center for Mendelian Genomics. 2014. RNF213 rare variants in an ethnically diverse population with Moyamoya disease. *Stroke.* 45:3200–3207. https://doi.org/10.1161/STROKEAHA.114.006244

Guey, S., M. Kraemer, D. Hervé, T. Ludwig, M. Kossorotoff, F. Bergametti, J.C. Schwitalla, S. Choi, L. Broseus, I. Callebaut, et al.;; FREX Consortium. 2017. Rare RNF213 variants in the C-terminal region encompassing the RING-finger domain are associated with moyamoya angiopathy in Caucasians. *Eur. J. Hum. Genet.* 25:995–1003. https://doi.org/10.1038/ejhg.2017.92

Kamada, F., Y. Aoki, A. Narisawa, Y. Abe, S. Komatsuzaki, A. Kikuchi, J. Kanno, T. Niihori, M. Ono, N. Ishii, et al. 2011. A genome-wide association study identifies RNF213 as the first Moyamoya disease gene. *J. Hum. Genet.* 56:34–40. https://doi.org/10.1038/jhg.2010.132

Kobayashi, H., Y. Matsuda, T. Hitomi, H. Okuda, H. Shioi, T. Matsuda, H. Imai, M. Sone, D. Taura, K.H. Harada, et al. 2015. Biochemical and Functional Characterization of RNF213 (Mysterin) R4810K, a Susceptibility Mutation of Moyamoya Disease, in Angiogenesis In Vitro and In Vivo. *J. Am. Heart Assoc.* 4:e002146. https://doi.org/10.1161/JAHA.115.002146

Koizumi, A., H. Kobayashi, T. Hitomi, K.H. Harada, T. Habu, and S. Youssefian. 2016. A new horizon of moyamoya disease and associated health risks explored through RNF213. *Environ. Health Prev. Med.* 21:55–70. https://doi.org/10.1007/s12199-015-0498-7

Kory, N., R.V. Farese Jr., and T.C. Walther. 2016. Targeting Fat: Mechanisms of Protein Localization to Lipid Droplets. *Trends Cell Biol.* 26:535–546. https://doi.org/10.1016/j.tcb.2016.02.007

Kotani, Y., D. Morito, S. Yamazaki, K. Ogino, K. Kawakami, S. Takashima, H. Hirata, and K. Nagata. 2015. Neuromuscular regulation in zebrafish by a large AAA+ ATPase/ubiquitin ligase, mysterin/RNF213. *Sci. Rep.* 5:16161. https://doi.org/10.1038/srep16161

Kotani, Y., D. Morito, K. Sakata, S. Ainuki, M. Sugihara, T. Hatta, S.-I. Iemura, S. Takashima, T. Natsume, and K. Nagata. 2017. Alternative exon skipping biases substrate preference of the deubiquitylase USP15 for mysterin/RNF213, the moyamoya disease susceptibility factor. *Sci. Rep.* 7:44293. https://doi.org/10.1038/srep44293

Krahmer, N., R.V. Farese Jr., and T.C. Walther. 2013. Balancing the fat: lipid droplets and human disease. *EMBO Mol. Med.* 5:973–983. https://doi.org/10.1002/emmm.201100671

Labbadia, J., and R.I. Morimoto. 2015. The biology of proteostasis in aging and disease. *Annu. Rev. Biochem.* 84:435–464. https://doi.org/10.1146/annurev-biochem-060614-033955

Liu, W., D. Morito, S. Takashima, Y. Mineharu, H. Kobayashi, T. Hitomi, H. Hashikata, N. Matsuura, S. Yamazaki, A. Toyoda, et al. 2011. Identification of RNF213 as a susceptibility gene for moyamoya disease and its possible role in vascular development. *PLoS One.* 6:e22542. https://doi.org/10.1371/journal.pone.0022542

Metzger, M.B., J.N. Pruneda, R.E. Klevit, and A.M. Weissman. 2014. RING-type E3 ligases: master manipulators of E2 ubiquitin-conjugating

enzymes and ubiquitination. *Biochim. Biophys. Acta.* 1843:47–60. https://doi.org/10.1016/j.bbamcr.2013.05.026

Morito, D., K. Nishikawa, J. Hoseki, A. Kitamura, Y. Kotani, K. Kiso, M. Kinjo, Y. Fujiyoshi, and K. Nagata. 2014. Moyamoya disease-associated protein mysterin/RNF213 is a novel AAA+ ATPase, which dynamically changes its oligomeric state. *Sci. Rep.* 4:4442. https://doi.org/10.1038/srep04442

Ogura, T., and A.J. Wilkinson. 2001. AAA+ superfamily ATPases: common structure--diverse function. *Genes Cells.* 6:575–597. https://doi.org/10.1046/j.1365-2443.2001.00447.x

Ohkubo, K., Y. Sakai, H. Inoue, S. Akamine, Y. Ishizaki, Y. Matsushita, M. Sanefuji, H. Torisu, K. Ihara, M. Sardiello, and T. Hara. 2015. Moyamoya disease susceptibility gene RNF213 links inflammatory and angiogenic signals in endothelial cells. *Sci. Rep.* 5:13191. https://doi.org/10.1038/srep13191

Raso, A., R. Biassoni, S. Mascelli, P. Nozza, E. Ugolotti, E. DI Marco, P. DE Marco, E. Merello, A. Cama, M. Pavanello, and V. Capra. 2016. Moyamoya vasculopathy shows a genetic mutational gradient decreasing from East to West. *J. Neurosurg. Sci.*

Scholz, B., C. Korn, J. Wojtarowicz, C. Mogler, I. Augustin, M. Boutros, C. Niehrs, and H.G. Augustin. 2016. Endothelial RSPO3 Controls Vascular Stability and Pruning through Non-canonical WNT/Ca(2+)/NFAT Signaling. *Dev. Cell.* 36:79–93. https://doi.org/10.1016/j.devcel.2015.12.015

Scott, R.M., and E.R. Smith. 2009. Moyamoya disease and moyamoya syndrome. *N. Engl. J. Med.* 360:1226–1237. https://doi.org/10.1056/NEJMra0804622

Soni, K.G., G.A. Mardones, R. Sougrat, E. Smirnova, C.L. Jackson, and J.S. Bonifacino. 2009. Coatomer-dependent protein delivery to lipid droplets. *J. Cell Sci.* 122:1834–1841. https://doi.org/10.1242/jcs.045849

Walther, T.C., and R.V. Farese Jr. 2012. Lipid droplets and cellular lipid metabolism. *Annu. Rev. Biochem.* 81:687–714. https://doi.org/10.1146/annurev-biochem-061009-102430

Wilfling, F., A.R. Thiam, M.-J. Olarte, J. Wang, R. Beck, T.J. Gould, E.S. Allgeyer, F. Pincet, J. Bewersdorf, R.V. Farese Jr., and T.C. Walther. 2014. Arf1/COPI machinery acts directly on lipid droplets and enables their connection to the ER for protein targeting. *eLife.* 3:e01607. https://doi.org/10.7554/eLife.01607

Zechner, R., F. Madeo, and D. Kratky. 2017. Cytosolic lipolysis and lipophagy: two sides of the same coin. *Nat. Rev. Mol. Cell Biol.* 18:671–684. https://doi.org/10.1038/nrm.2017.76

Zimmermann, R., J.G. Strauss, G. Haemmerle, G. Schoiswohl, R. Birner-Gruenberger, M. Riederer, A. Lass, G. Neuberger, F. Eisenhaber, A. Hermetter, and R. Zechner. 2004. Fat Mobilization in Adipose Tissue Is Promoted by Adipose Triglyceride Lipase. *Science.* 306:1383–1386.